Subgrid Surface Fluxes in Fair Weather Conditions during TOGA COARE: Observational Estimates and Parameterization

DEAN VICKERS AND STEVEN K. ESBENSEN

College of Oceanic and Atmospheric Sciences, Oregon State University, Corvallis, Oregon

ABSTRACT

Bulk aerodynamic formulas are applied to meteorological data from low-altitude aircraft flights to obtain observational estimates of the subgrid enhancement of momentum, sensible heat, and latent heat exchange at the atmospheric–oceanic boundary in light wind, fair weather conditions during TOGA COARE (Tropical Ocean Global Atmosphere Coupled Ocean–Atmosphere Response Experiment). Here, subgrid enhancement refers to the contributions of unresolved disturbances to the grid-box average fluxes at the lower boundary of an atmospheric general circulation model. The observed subgrid fluxes increase with grid-box area, reaching 11%, 9%, 24%, and 12% of the total sensible heat, latent heat, scalar wind stress, and vector wind stress magnitude, respectively, at a grid-box size of $2° \times 2°$ longitude and latitude.

Consistent with previous observational and modeling studies over the open ocean, most of the subgrid flux is explained by unresolved directional variability in the near-surface wind field. The authors find that much of the observed variability in the wind field in the presence of fair weather convective bands and patches comes from contributions of curvature and speed variations of simple larger-scale structure across the grid box.

Inclusion of a grid-scale-dependent subgrid velocity scale in the bulk aerodynamic formulas effectively parameterizes the subgrid enhancement of the sensible heat flux, latent heat flux, and vector stress magnitude, and to a lesser degree the subgrid enhancement of the scalar wind stress. An observational estimate of the subgrid velocity scale derived from one-dimensional aircraft flight legs is found to be smaller than that derived from a two-dimensional grid-box analysis. The additional enhancement in the two-dimensional case is caused by the nonhomogeneous and nonisotropic characteristics of the subgrid-scale wind variability. Long time series from surface-based platforms in the TOGA COARE region suggest that measures of convective activity, in addition to geometric grid-scale parameters, will be required to more accurately represent the subgrid velocity scales.

1. Introduction

The specific scientific objectives of TOGA COARE (Tropical Ocean Global Atmosphere Coupled Ocean–Atmosphere Response Experiment) include understanding ocean–atmosphere exchanges of heat, moisture, and momentum over a variety of timescales in the western Pacific warm-pool region and improving the empirical formulas for estimating these exchanges in large-scale numerical models (World Climate Research Program 1990). This study focuses on the enhancement of surface fluxes by atmospheric disturbances that would be unresolved within a grid box of a large-scale general circulation model. The analysis is based on observations taken during relatively undisturbed conditions during TOGA COARE.

The surface fluxes of the alongwind stress component τ, the sensible heat H, and the latent heat E averaged over a spatial area corresponding to a numerical model grid box, may be estimated by the vertical eddy fluxes in a thin layer above the surface, that is,

$$\tau = -\rho\langle\overline{w'u'}\rangle \tag{1}$$

$$H = \rho c_p\langle\overline{w'\theta'}\rangle \tag{2}$$

$$E = \rho L_v\langle\overline{w'q'}\rangle. \tag{3}$$

Here, w is the vertical component of the wind, u the wind speed in the mean downwind direction, θ the potential temperature, q the specific humidity, ρ the air density, c_p the specific heat at constant pressure, and L_v the latent heat of evaporation. For convenience, we will ignore the small contribution of the variations of ρ, c_p, and L_v to the estimate of the fluxes throughout this paper [see Sun et al. (1996) for discussion]. The definition of the wind stress varies in the literature, usually meaning either the upwind component alone [Eq. (1)] or the magnitude of the total stress vector, which includes the crosswind component.

The overbar in Eqs. (1)–(3) refers to a local mean over a temporal or spatial domain that is just large enough to contain a representative sample of the turbulent elements responsible for most of the vertical flux,

Corresponding author address: Dean Vickers, College of Oceanic and Atmospheric Sciences, Oregon State University, Corvallis, OR 97331-5503.
E-mail: vickers@ats.orst.edu

and the prime denotes deviations from the local mean. The angle brackets refer to a spatial average over the grid-box domain. Based on the work of Sun et al. (1996), and our own sensitivity tests, we will use spatial averages over 10-km aircraft flight segments as the scale appropriate to capture most of the surface flux. Selection of the local averaging scale is nevertheless rather arbitrary since there is no clear separation between the flux contributions of turbulent and mesoscale disturbances in the atmospheric boundary layer.

The standard bulk aerodynamic formula for the surface flux of a quantity ϕ (i.e., U, θ, or q) has the form

$$F_\phi = \rho C_\phi U(\overline{\phi}_{\text{sfc}} - \overline{\phi}), \qquad (4)$$

where U is a wind speed relative to the surface (moving, in the case of the ocean), $\overline{\phi}_{\text{sfc}}$ is the value of $\overline{\phi}$ at the surface, and C_ϕ is a bulk aerodynamic transfer coefficient based on similarity theory. In this study, we will use the COARE 2.5a algorithm of Fairall et al. (1996), which was developed to improve the representation of surface fluxes in the unstable light-wind conditions often found over the western Pacific warm-pool region. The COARE algorithm is based on Monin–Obukhov similarity theory.

We note that the definition of U is problematic because of the wind's vector nature. Here we distinguish between the magnitude of the local mean vector wind U and the scalar mean of the instantaneous wind speed S defined, respectively, as

$$U = (\overline{u}^2 + \overline{v}^2)^{1/2} \qquad (5)$$

$$S = \overline{(u^2 + v^2)^{1/2}}. \qquad (6)$$

The COARE bulk algorithm is designed to accept the magnitude of the local mean vector wind U as the input velocity scale, not S. In the algorithm, the input velocity U is enhanced by a convective velocity scale using the parameterization of Godfrey and Beljaars (1991) and Beljaars (1995) to account for wind direction variability due to free convection [Fairall et al. 1996; Eq. (15)]. We interpret this convective velocity scale as a representation of variability in the wind on scales less than about 10 km due to the presence of free convection. The effective velocity scale in the bulk algorithm, $\hat{S}$, is given by

$$\hat{S}^2 = U^2 + w_g^2, \qquad (7)$$

where w_g is proportional to the convective scaling velocity w_*. The assumptions made in deriving Eq. (7) are discussed in Mahrt and Sun (1995a). In the COARE algorithm, the effective velocity scale $\hat{S}$ is used explicitly as the velocity scale for calculating the Monin–Obukov length and other similarity parameters, and ultimately, the fluxes. Equation (4) should therefore be viewed as a symbolic representation of the complicated operator actually used in the flux computation.

In general, the surface flux of a quantity ϕ will vary over spatial scales smaller than the resolution of a large-

scale numerical model. The model must predict the spatial average fluxes $\langle F_\phi \rangle$ from a knowledge of explicit spatial averaged model variables or parameterized quantities based on explicit model variables. The explicitly resolved variables of a large-scale model typically include the areally averaged wind vector **V,** the sea surface temperature, and the air temperature and humidity. The grid-box average magnitude of the local mean wind vector $\langle U \rangle$ is typically not available in large-scale numerical models.

Assuming that bulk aerodynamic parameterizations of the surface flux adequately represent the local mean surface fluxes, the problem of parameterizing the grid-box average surface fluxes may be reduced to the problem of determining an effective transfer coefficient $\hat{C}_\phi$ in the expression

$$\langle F_\phi \rangle = \rho \hat{C}_\phi V(\langle \overline{\phi}_{\text{sfc}} \rangle - \langle \overline{\phi} \rangle) \qquad (8)$$

where

$$V \equiv (\langle u \rangle^2 + \langle v \rangle^2)^{1/2} \qquad (9)$$

is the magnitude of the grid-box-averaged vector wind. Therefore, $\hat{C}_\phi$ includes all nonlinear effects of subgrid-scale disturbances and variability. In general, the effective transfer coefficient $\hat{C}_\phi$ is not the same as the areally averaged transfer coefficient $\langle C_\phi \rangle$. For example, the magnitude of the areally averaged wind vector can approach zero while the areally averaged surface fluxes can be nonzero. In this case, the effective transfer coefficient in Eq. (8) must approach infinity while the average transfer coefficient remains finite.

An alternative to using an effective transfer coefficient formulation [Eq. (8)] is to introduce a subgrid velocity scale V_{sg} and evaluate the spatial average surface flux in terms of the local mean transfer coefficient based on similarity theory and an effective velocity scale, $(V^2 + V_{\text{sg}}^2)^{1/2}$, namely,

$$\langle F_\phi \rangle = \rho C_\phi (V^2 + V_{\text{sg}}^2)^{1/2}(\langle \overline{\phi}_{\text{sfc}} \rangle - \langle \overline{\phi} \rangle) \qquad (10)$$

[e.g., Mahrt and Sun (1995a)]. As in Eq. (4), the convective velocity scale (w_g) used in the COARE algorithm for estimating local mean (e.g., 10-km scale) surface fluxes is implicit in Eq. (10). For example, the total effective velocity scale S used by the bulk algorithm for a value of $V_{\text{sg}} = 1.5$ m s^{-1}, a model resolved vector wind of 4 m s^{-1}, and a typical value of the implicit convective velocity scale of 0.8 m s^{-1}, would be

$$S = (V^2 + w_g^2 + V_{\text{sg}}^2)^{1/2}$$
$$= (4^2 + 0.8^2 + 1.5^2)^{1/2} = 4.3 \text{ m s}^{-1}. \qquad (11)$$

Observationally, the subgrid velocity scale can be related to the spatial averaged magnitude of the local mean wind, $\langle U \rangle$, and the magnitude of the model resolved wind by

$$V_{\text{sg}}^2 = \langle U \rangle^2 - V^2. \qquad (12)$$

In a numerical model, the squared subgrid velocity scale

would be parameterized as the difference between the square of the grid-box average local mean velocity, $\langle U \rangle^2$, some or all of which may not be resolved by the model grid, and the square of the model-resolved wind, V^2.

For simplicity, we will symbolize the bulk formula for the wind stress, sensible heat, and latent heat fluxes by an algorithm or function, $\mathcal{F}$, which, given a set of meteorological input variables and a method (similarity theory) for estimating the transfer coefficients, will return the corresponding surface fluxes. The fluxes are written symbolically as

$$\mathbf{F} = \mathcal{F}(U, \overline{\theta}_{\text{sfc}}, \overline{\theta}, \overline{q}), \qquad (13)$$

where $\mathbf{F} \equiv (F_\tau, F_H, F_E)$ is the wind stress, the sensible heat, and the latent heat flux, respectively. In this study, $\mathcal{F}$ represents the COARE bulk flux algorithm. The actual COARE algorithm has additional input variables we have not included explicitly in Eq. (13), such as the height of the observations, but these parameters are not the primary focus of our study.

We can now give a more precise definition of subgrid enhancement of the surface fluxes. Assuming the bulk algorithm is an accurate parameterization of the local mean turbulent surface flux, the "true" grid-box average flux may be written as

$$\mathbf{F}_{\text{true}} = \langle \mathcal{F}(U, \overline{\theta}_{\text{sfc}}, \overline{\theta}, \overline{q}) \rangle, \qquad (14)$$

which is the grid-box average of all the local mean fluxes. The flux that would be calculated by a large-scale model without a parameterization of the subgrid flux is written as

$$\mathbf{F}_{\text{model}} = \mathcal{F}(V, \langle \overline{\theta}_{\text{sfc}} \rangle, \langle \overline{\theta} \rangle, \langle \overline{q} \rangle). \qquad (15)$$

The subgrid flux is then defined as

$$\mathbf{F}_{\text{subgrid}} = \mathbf{F}_{\text{true}} - \mathbf{F}_{\text{model}}. \qquad (16)$$

Subgrid flux does not include flux directly attributable to mesoscale fluctuations, but does include mesoscale modulation of the local turbulent fluxes.

In this study we show that a parameterization for V_{sg} as a function of grid-box size can represent the subgrid flux observed in fair weather conditions over the Pacific warm pool in TOGA COARE. Although intuition might suggest that the subgrid enhancement of surface fluxes would be insignificant in fair weather conditions, we find that this is not the case during TOGA COARE. It will be shown that the enhancement is due both to physical subgrid-scale disturbances, as well as simple larger-scale structure across the grid box.

In the first part of this study, we check the validity of using aircraft data in the 25–100-m layer above the sea surface to estimate surface fluxes using the COARE bulk algorithm. The observational datasets, the quality control testing of the fast response NCAR Electra turbulence data, and an intercomparison of observations from the Electra and two NOAA P3 aircraft are described in section 2. In section 3, we evaluate the pa-

rameterized bulk flux calculated from measurements on board the three aircraft by comparing to direct turbulence measurements and bulk fluxes from two surface platforms.

In the second part of this study, we use bulk flux estimates from the aircraft data to estimate subgrid fluxes. In section 4, meteorological measurements from three aircraft are used in the COARE bulk flux algorithm to spatially map local mean surface fluxes of momentum, sensible heat, and latent heat onto simulated grid boxes of varying resolution. The observed subgrid fluxes and subgrid velocity scale are presented in section 5. Some issues related to parameterization of subgrid fluxes are discussed in section 6.

2. Datasets

The observational datasets used in this study are discussed briefly in this section. The datasets include aircraft and surface-based observations made in the IFA (intensive flux array) region during the IOP (intensive observing period) of TOGA COARE.

a. NOAA WP3D aircraft

The 1-Hz NOAA WP3D data for the *N42RF* and *N43RF* aircraft were obtained from the University of California at Irvine (UCI). These data include all the processing performed and documented by Dr. C. A. Friehe's group as of 18 July 1996. The UCI data fields selected to represent the horizontal wind components u and v, air temperature T, specific humidity q, sea surface radiative temperature T_{sfc}, latitude, longitude, pressure, and aircraft altitude were wxff1, wyff1, tad f2, sh gef, trdprt, latilc, longilc, psfc, and hr232, respectively. We added 0.3°C to all P3 air temperatures based on the empirical offsets determined by S. Burns, D. Khelif, and C. Friehe (1997, personal communication).

b. NCAR Electra aircraft

The 1- and 20-Hz NCAR Electra data were obtained from the archives at NCAR. These data include all NCAR processing performed as of March 1996. The selected Electra data fields included the horizontal and vertical wind components, air temperature, dewpoint temperature, sea surface radiative temperature, latitude, longitude, pressure, and aircraft altitude with data field names xuc, xvc, xwc, atb, dptc, rstb, glat, glon, psfdc, and hgm, respectively. For eddy correlation latent heat flux calculations, the UV hygrometer instrument (xmruv) was used for flights RF01–RF19, and the Lyman-alpha (mrla) for flights RF20–RF32. The slow response dewpointer (dptc) was used for humidity in the bulk flux calculations. We applied corrections to the Electra slow response dewpoint temperature and sea surface radiative temperature and to fast-response air temperature based on intercomparison results from S.

Burns, D. Khelif, C. Friehe (1997, personal communication). These corrections include 1) adding $-0.1°C$ to the dewpoint temperature for flight RF03; 2) adding $0.05C$, $-0.2°C$, and $-0.3°C$ to the air temperature for flights RF02–RF03, RF04, and RF05–RF32, respectively; and 3) adding $-0.7°C$ to the sea surface radiative temperature for all flights.

c. IMET

Processed data from the IMET mooring (located at $1.75°S$, $156°E$) were obtained from Dr. R. Weller of the Woods Hole Oceanographic Institution. The data represent simultaneous 7.5-min averages for the period 21 October 1992 through 4 March 1993. The wind components used in our IMET bulk flux calculations are the relative velocity shear between the wind and the moving surface. The incoming shortwave and outgoing longwave radiation measurements permit an estimate of the ocean skin temperature T_{sfc}, using the subsurface measurement (0.45 m below the surface) and the cool skin and warm layer temperature model in the COARE bulk algorithm. The IMET winds, air temperature, and humidity are measured at heights of 3.4, 2.8, and 2.8 m, respectively. Air temperature (IMET data field atmp) is thought to be suspect (overestimated) during clear sky and light wind speed conditions because of solar heating effects. Therefore, IMET data periods with light winds are not included in our analysis.

d. R/V Moana Wave

The *Moana Wave* data used in this study were obtained from Dr. C. Fairall at ETL NOAA in September 1996. All processing of these data has been described in the documentation of C. Fairall for the R/V *Moana Wave* Flux Data (Release 2.5). Data were taken during three periods: 11 November to 3 December 1992, 17 December 1992 to 11 January 1993, and 28 January to 16 February 1993. The ship was normally located near $1.7°S$, $156.0°E$. The data fields are means and fluxes averaged over 50-min time periods. The winds, air temperature, and humidity are all measured at a height 15 m above the sea surface.

e. Aircraft data processing

The fast-response Electra variables used for calculating eddy correlation fluxes were subjected to the quality control screening procedures developed by Vickers and Mahrt (1997). Of the low-level (<100 m) Electra flight legs considered in this study, only 10 legs were discarded due to instrument problems. In the majority of these cases, the humidity (UV hygrometer) was found to have intermittent problems. Twelve legs were retained but truncated to remove suspect data. In several of these cases it appears that the air temperature (atb) and the humidity instrument were not in equilibrium with am-

TABLE 1. Aircraft mission dates included in the analysis and number of low-level 10-km flight segments found for each. TOGA convective class 2, 3, and 4 flight days are intentionally excluded.

Date	Class	N42RF	N43RF	Electra
2 Nov 92	1	89	86	0
13 Nov 92	0	72	98	0
15 Nov 92	0	0	78	65
26 Nov 92	1	62	115	45
28 Nov 92	0	44	78	43
2 Dec 92	0	0	0	18
3 Dec 92	0	0	0	27
4 Dec 92	0	0	0	13
6 Dec 92	0	0	0	11
8 Dec 92	1	0	0	23
9 Dec 92	1	0	0	64
10 Dec 92	0	0	0	31
16 Dec 92	1	52	89	54
9 Jan 93	1	79	107	48
11 Jan 93	0/1	45	0	0
12 Jan 93	1	0	0	6
13 Jan 93	0	0	0	20
14 Jan 93	0	0	0	16
16 Jan 93	1	65	3	0
17 Jan 93	1	51	55	34
18 Jan 93	1	58	27	10
26 Jan 93	0	0	0	8
27 Jan 93	0	0	0	12
28 Jan 93	0	0	0	21
1 Feb 93	0	63	0	0
17 Feb 93	1	18	0	0
19 Feb 93	0	0	81	0

bient conditions following an aircraft descent, and the suspect data was removed by discarding the flagged portion of the leg.

The NOAA–UCI and NCAR Electra aircraft data were processed to find flight legs when the aircraft were flying at nearly constant altitude at or below 100 m above the sea surface. For these legs, local means were calculated for all contiguous 10-km segments in the leg. The number of low-level 10-km flight segments found for each aircraft for each flight mission is shown in Table 1. Flights on days with widespread intense convective activity in the IFA, classified here as class 2 or higher, are excluded from our analysis and from Table 1.

We choose to exclude flight days classified as having intense convection to estimate the fair weather, or relatively undisturbed, subgrid flux enhancement. We expect that the subgrid enhancement during periods of intense convection will be larger than in undisturbed conditions (Johnson and Nicholls 1983), and that the enhancement will be a strong function of the relative position of the aircraft flight tracks within the convective systems. For example, we would expect the enhancement to be quite different depending on whether the aircraft were sampling along a flight track parallel or perpendicular to a convective line. Therefore, the sampling problems in analyzing the disturbed cases are likely to be more severe. We feel that these aircraft data alone are insufficient to obtain statistically significant results for the disturbed case.

TABLE 2. Electra eddy correlation composite fluxes. The values shown for this study are the mean of 569 10-km mean values for all flights in Table 1. Values from Sun (Sun et al. 1996) and Rogers (Fairall et al. 1996) are shown for comparison.

Source	L	λ	E	H	τ
This study	1	10	73	5.3	1.5
This study	10	10	83	6.7	1.6
Sun	1	60–130	68	5.1	1.9
Sun	5	60–130	78	5.9	1.8
Sun	60–130	60–130	86	4.5	1.6
Rogers			76	6.0	1.8

TABLE 3. Bulk and eddy correlation composite flux values from various measurement platforms and investigators. The values shown for this study are the mean of 569 10-km mean values for all flights in Table 1.

Source	Method	E	H	τ
Fairall, *Moana Wave*	Bulk	94	5.7	3.3
Fairall, *Moana Wave*	Eddy	94	8.2	3.1
Rogers, Electra	Bulk	81	6.0	1.8
Rogers, Electra	Eddy	76	6.0	1.8
This study, Electra	Bulk	96	6.5	2.1
This study, Electra	Eddy	83	6.7	1.6

f. Aircraft intercomparison

Detailed TOGA COARE surface-to-aircraft and aircraft-to-aircraft intercomparisons have been performed by S. Burns, D. Khelif, and C. Friehe (1997, personal communication). As an independent check for our own purposes, we intercompared air temperature, surface radiative temperature, specific humidity, and wind speed from the three aircraft by comparing the arithmetic average of all low-level 10-km local means within the IFA for each of the intercomparison flight days in Table 1.

The largest discrepancies are the high Electra air temperature on 16 December compared to the two P3s, and on 9 January the low Electra air temperature and surface radiative temperature compared to the two P3s. On 16 December (9 January) the Electra was farther south than the two P3s, which could explain the warmer (cooler) air temperature. We conclude from this simple intercomparison that the aircraft measurements agree with each other well enough to combine them for the purpose of mapping local fluxes without introducing artificial variability due to different instrumentation and processing for each aircraft.

3. Bulk and eddy fluxes

As a check on the validity of the COARE algorithm (Fairall et al. 1996), in this section we compare parameterized bulk fluxes to fluxes calculated from direct turbulence measurements on the Electra. In addition, bulk and eddy fluxes from all the aircraft measurements are compared with bulk fluxes from the IMET mooring and bulk and covariance fluxes from the R/V *Moana Wave* during aircraft flyovers. A detailed comparison of bulk and eddy flux estimates from all surface and aircraft platforms in the TOGA COARE IFA during the IOP has been made by S. Burns, D. Khelif and C. Friehe (1997, personal communication).

a. Eddy correlation fluxes

Our eddy correlation method requires specification of two length or averaging scales: L, the local averaging scale for defining the turbulent fluctuations from the mean, and λ, the flux averaging scale (Sun et al. 1996). Turbulent fluctuations of some quantity, ϕ, are defined as deviations from a local mean, $\overline{\phi}$, and the decomposition of ϕ can then be written as

$$\phi = \overline{\phi} + \phi', \qquad (17)$$

where $\overline{\phi}$ is an average over length scale L. The averaging length L defines the longest length scales of motion included in the flux. The quantity ϕ is the alongwind component of the wind for calculating the wind stress, the potential temperature for the sensible heat flux, and the specific humidity for the latent heat flux. The product of the fluctuations of ϕ' and the vertical velocity fluctuations w' are averaged over the flux averaging length scale λ to calculate the local mean flux. The flux averaging scale should be chosen large enough to reduce the random sampling error but short enough to avoid including mesoscale variability and nonstationarity effects (Mahrt et al. 1996; Sun et al. 1996). The sensitivity of the flux to the choice of L is demonstrated in Table 2.

We select a local averaging scale $L = 10$ km to define the turbulent fluctuations and a flux averaging scale $\lambda = 10$ km for averaging the products of the perturbations. These choices are based on our goals of capturing the majority of the turbulent and large-eddy scale flux (Sun et al. 1996), while still retaining a 10-km spatial resolution for evaluating the subgrid flux. The 10-km averaging scale is also consistent with the temporal averaging scale (50 min) used in the development of the COARE bulk flux algorithm. We will present only statistical results, however, since even in fair weather conditions a single one-dimensional 10-km flight leg is probably an inadequate spatial sample of the main transporting eddies. Ideally, repeated legs over the same flight track would be used to average the flux and reduce the random error without sacrificing spatial resolution, but these observations are not available.

b. Bulk and eddy flux comparisons

Composite bulk and eddy flux estimates during TOGA COARE reported by Fairall et al. (1996) and from this study are presented in Table 3. The composites include all observational records selected by each study during the COARE IOP and vary by study. All our fluxes are calculated using $L = \lambda = 10$ km, and use constant values for the density of air (1.16 kg m^{-3}), the

heat capacity of dry air at constant pressure (1005 *J* kg^{-1} K^{-1}), and the latent heat of evaporation (2400 kJ kg^{-1}). Intercomparison of the *Moana Wave* and Electra fluxes is complicated by the different observation days and times included in the various composites.

The *Moana Wave* ship-based fluxes from Fairall et al. (1996) are the basis for the development of the COARE bulk flux algorithm and are derived from 50-min records of ship deck-level (15 m) bulk and fast-response covariance measurements and floating thermometer sea temperature measurements. The composite bulk and covariance *Moana Wave* latent heat fluxes reported by Fairall et al. (1996) agree (Table 3). This agreement of the two composite means is presumably due to the calibration of the COARE bulk flux algorithm using the *Moana Wave* turbulence measurements.

Our composite fluxes calculated using the Electra data show that the sensible heat flux, latent heat flux, and wind stress from the bulk algorithm are −3%, 16%, and 31% larger, respectively, than those from the eddy correlation technique. The standard error of each estimate is small compared to the mean difference between the bulk and eddy flux. The positive difference between the bulk and the eddy correlation estimate of the fluxes increases with increasing wind speed (Figs. 1a–c). For wind speeds less than about 5 m s^{-1}, the parameterized bulk fluxes agree quite well with the eddy correlation fluxes, however, the scatter between the two estimates of the flux for an individual 10-km local mean can be large (Figs. 2a–c).

A comparison of bulk and eddy correlation fluxes during periods when the Electra was flying over the *Moana Wave* is shown in Table 4. Flyovers are defined when the midpoint of a 10-km aircraft flight segment is located within 20 km of the surface platform and when the aircraft observation time is within 30 min of the surface observation time. The conditions during the flyovers in Table 4 include 15-m wind speeds ranging from 1 to 5 m s^{-1}, 15-m air temperatures from 27° to 29°C, 15-m specific humidities from 17.5 to 18.7 g kg^{-1}, and water skin temperatures from 29° to 31°C. With the exception of the Electra's small eddy correlation wind stress and large bulk latent heat flux, the fluxes generally agree; however, the bulk latent heat flux from the aircraft is 15% larger than the bulk flux from the ship.

Bulk and eddy correlation fluxes during Electra flyovers of the IMET mooring are shown in Table 5. The IMET flyovers were only included in the Table 5 composites when the IMET 3.4-m wind speed exceeded 3 m s^{-1}. The conditions during the flyovers include 3.4-m wind speeds ranging from 3 to 7 m s^{-1}, 2.8-m air temperatures from 27° to 30°C, 2.8-m specific humidities from 20.0 to 21.9 g kg^{-1}, and water skin temperatures from 29° to 30°C. Similar to the Electra and *Moana Wave* comparison, these results show that in general the aircraft bulk latent heat fluxes are larger than bulk latent heat fluxes calculated from the near-surface
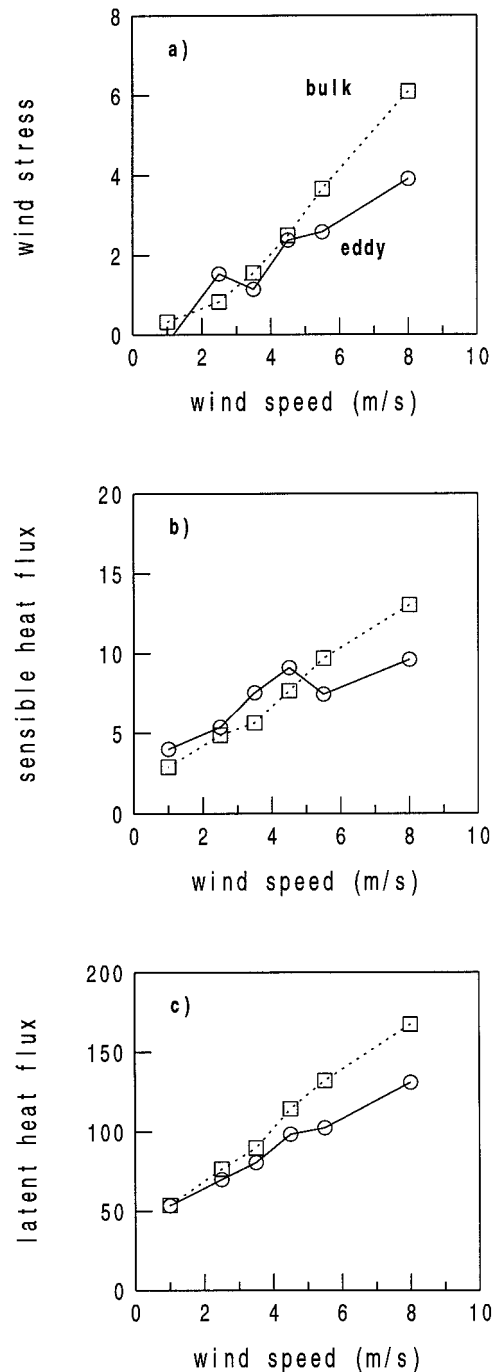

FIG. 1. Wind speed dependence of the bulk (squares and dashed) and eddy correlation (circles and solid) fluxes calculated from measurements on the NCAR Electra aircraft for (a) scalar wind stress ($\times 10^{-2}$ m^2 s^{-2}), (b) sensible heat (W m^{-2}), and (c) latent heat (W m^{-2}).

platform, and that the aircraft bulk fluxes are larger than the aircraft eddy correlation fluxes.

One factor that might explain part of the bias between the aircraft bulk and eddy correlation fluxes is the known
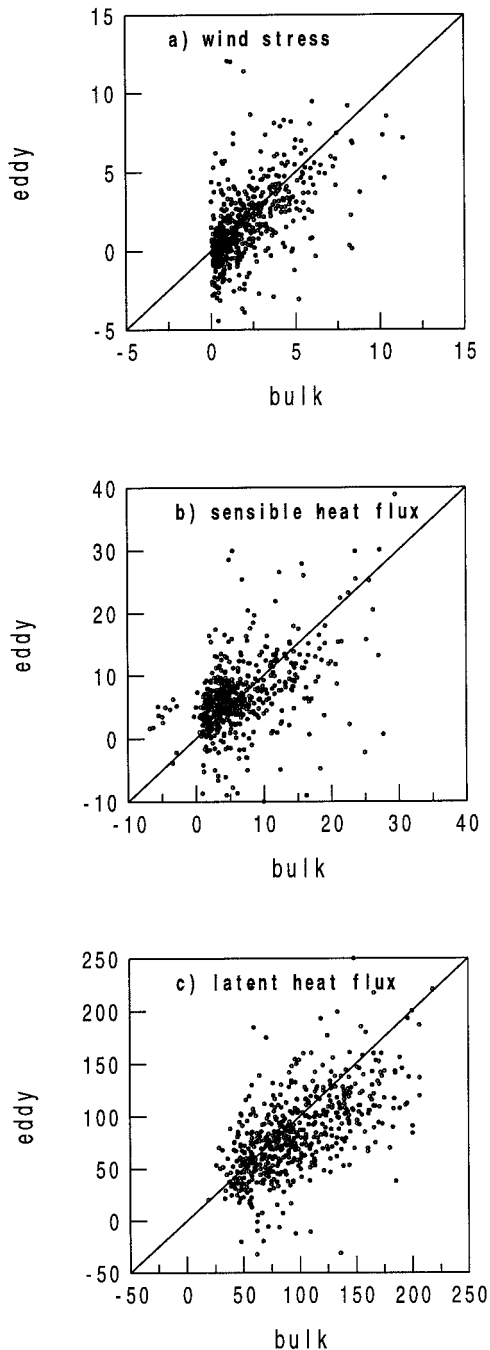
FIG. 2. Bulk versus eddy correlation fluxes calculated from measurements on the NCAR Electra aircraft for (a) scalar wind stress ($\times 10^{-2}$ m^2 s^{-2}), (b) sensible heat (W m^{-2}), and (c) latent heat (W m^{-2}).

TABLE 4. Composite bulk and eddy correlation fluxes for 29 Electra flyovers of the *Moana Wave.*

Source	E	H	τ
Moana Wave, bulk	83	7	1.3
Electra, bulk	95	7	1.4
Moana Wave, eddy	89	8	1.4
Electra, eddy	86	6	0.5

our choice of $L = 10$ km and a measurement height of 30–100 m.

Another factor that may bias our bulk and eddy correlation flux comparison could be instrument calibration and drift problems on the Electra. A constant additive offset to the air temperature, humidity, or sea surface radiative temperature would not significantly effect the eddy correlation flux. If, however, the air temperature (humidity) was lower than actual, the bulk fluxes would be larger than actual, since the temperature (humidity) difference, $T_{sfc} - T$ ($q_{sfc} - q$), used in the bulk parameterization would be larger. Similarly, if the surface radiative temperature was higher than actual, the bulk fluxes would be larger than actual. The Electra sea surface temperature measurement (PRT5 instrument) is the most suspect (C. Friehe 1996, personal communication).

c. Bulk aircraft and near-surface bulk fluxes

Composite bulk fluxes from the aircraft and the *Moana Wave* during aircraft flyovers are shown in Table 6. The largest discrepancies with the *Moana Wave* bulk fluxes are for the large Electra latent heat flux and the small P3 N42 wind stress. Analysis of aircraft flyovers of the IMET mooring (Table 7) shows generally larger flux discrepancies than found for the *Moana Wave.*

A possible explanation as to why the bulk latent heat fluxes from the aircraft are large compared to the *Moana Wave* and IMET mooring is that the profile functions in the bulk algorithm are not strictly valid when applied from the surface up to aircraft height. The similarity theory profiles are formally valid only in the atmospheric surface layer, up to a height on the order of the Monin–Obukov length scale, below which shear effects dominate buoyancy effects in the turbulence kinetic energy budget. Calculation of the Monin–Obukov length from either the low-altitude Electra data or the *Moana Wave* or IMET data shows that the surface layer is shallow (typically 10 m) over the warm pool during undisturbed conditions in COARE, due to generally light

increase in the scale of the transporting eddies with height above the surface. The length scale for defining the turbulent fluctuations, *L,* must increase with measurement height to capture an equivalent portion of the total flux (Williams et al. 1996) in a constant flux layer. However, we do not expect this effect to be large for

TABLE 5. Composite bulk and eddy correlation fluxes for 12 Electra flyovers of the IMET mooring.

Source	E	H	τ
IMET, bulk	98	7	3.5
Electra, bulk	117	8	3.7
Electra, eddy	98	7	1.6

TABLE 6. Composite bulk fluxes for aircraft (P3 N42, P3 N43, Electra) flyovers of the *Moana Wave* with N being the number of flyovers included in each composite.

Source	N	E	H	τ
Moana Wave	90	107	14	3.8
P3 N42	90	109	11	2.8
Moana Wave	79	87	8	1.6
P3 N43	79	98	7	1.5
Moana Wave	32	82	7	1.2
Electra	32	95	6	1.5
Moana Wave	201	95	10	2.5
All 3 aircraft	201	102	9	2.1

TABLE 7. Composite bulk fluxes for aircraft (P3 N42, P3 N43, Electra) flyovers of the IMET mooring with N being the number of flyovers included in the composite.

Source	N	E	H	τ
IMET	63	125	11	6.0
P3 N42	63	151	13	5.4
IMET	41	105	7	4.8
P3 N43	41	141	12	4.0
IMET	12	98	7	3.5
Electra	12	117	8	3.7
IMET	116	115	9	5.3
All 3 aircraft	116	144	12	4.7

winds and large fluxes of latent heat. We find that the three aircraft are sampling above the surface layer 90% of the time, even when flying at the lowest altitudes (25–50 m). Above the surface boundary layer, the profile of temperature and humidity may be influenced by processes not accounted for in Monin–Obukov similarity theory.

Considering that the aircraft are nearly always flying above the surface boundary layer, that the aircraft data are a one-dimensional spatial average along flight tracks while the stationary surface-based platforms are temporal averages of the flow past the platform, and that our flux comparisons include all unknown and remaining unresolved instrumentation problems on the three aircraft, the *Moana Wave,* and the IMET mooring, the bulk estimates of the fluxes from the aircraft and the surface-based platforms agree quite well. For the remainder of this study we will assume that bulk fluxes calculated from aircraft data provide a reasonable estimate of the true surface flux, which will enable mapping surface fluxes for an evaluation of the subgrid flux.

4. Subgrid analysis method

The goal of our grid-box analysis is to map observations from the three aircraft onto large spatial regions representative of a grid box in a large-scale numerical model. When adequately sampled regions are found, an estimate can be made of the subgrid contributions to the grid-box average flux.

Our automated procedure steps through a series of potentially usable grid boxes that are uniformly distributed in space and time over the IFA, and maps the aircraft 10-km local-mean data onto each grid box. Seven different grid-box resolutions are included: 0.65, 0.75, 1.00, 1.25, 1.50, 1.75, and 2.00, in spatial units of degrees of longitude and latitude and in temporal units of hours. Finer resolutions were tested, but not enough grid boxes were found that met our sampling requirements (see below). Each 10-km local-mean observation from an aircraft is mapped onto a potential grid box if the mean spatial location of the flight segment is inside the grid box and the mean time is within plus or minus one-half the temporal resolution from the grid-box-centered time. Our compositing technique (see below) will account for the fact that different grid boxes may contain many of the same local mean data points, and therefore may not be independent realizations. All data within the time window of the grid box are considered to be simultaneous, and altitude variations within the 25–100-m layer above the sea surface are ignored.

The local means inside a potential grid box are mapped into 16 equally sized spatial scenes. The grid-box is considered "adequately sampled" for the purpose of calculating the subgrid flux if at least 7 out of 12 of the exterior scenes and 2 out of 4 of the interior scenes contain at least one observation. The combined exterior and interior scene requirements ensure that the data is reasonably distributed over the grid box, and that more than one-half the scenes are sampled.

For adequately sampled grid boxes, the local means inside the grid box are nonuniformly weighted when calculating the grid-box average because the data are not uniformly distributed within the grid box. Our technique weights each local mean in the grid box inversely proportional to the number of local mean data points in the scene containing it. This is equivalent to first calculating the individual scene averages and then averaging the scenes with equal weights to produce a grid-box average, and gives a more accurate representation of the spatial variability within the grid box than a technique that averages all local means in the grid box with equal weight.

The values of $\mathbf{F}_{\text{true}}$ [Eq. (14)] and $\mathbf{F}_{\text{model}}$ [Eq. (15)] are calculated for each adequately sampled grid box. The flux difference, true minus model, is an observational estimate of the subgrid flux, $\mathbf{F}_{\text{subgrid}}$. Individual estimates of the true and model fluxes are composited separately for each resolution using nonoverlapping 1-h periods. The 1-h averaging period is chosen because the automated procedure often selects several grid boxes that are not fully independent because a large fraction of the 10-km local means in one grid box are also contained in another grid box that has a slightly different spatial or temporal location. The 1-h averaging combines these dependent grid boxes into a single "realization." The composite at each resolution is constructed by averaging the 1-h realizations over the entire observation record.

Sensitivity tests show that our composites are basically unchanged when using 0.5-, 2-, or 4-h averaging instead of 1 h.

With an ideal set of aircraft flight tracks and a perfect analysis method we would expect the composited true flux to be independent of grid scale. That is, we would want the grid boxes at each resolution to be drawn from the same population and the smaller grid boxes to be subregions of the larger grid boxes. If, however, the larger grid boxes were adequately sampled only on days with light winds, the true flux might decrease with grid scale. This type of sampling problem could affect our estimate of the subgrid flux. To reduce this sampling problem, we impose the condition that the composites include only those flight days for which a significant number of grid boxes were found at all tested resolutions. There are seven different flight days where adequately sampled grid boxes at all resolutions are found: 2 November, 13 November, 15 November, 26 November, 16 December 1992, 9 January and 17 January 1993.

The composite subgrid flux is defined as

$$[\mathbf{F}_{\text{subgrid}}] = [\mathbf{F}_{\text{true}}] - [\mathbf{F}_{\text{model}}], \quad (18)$$

where the square brackets represent the compositing method discussed above. The relative contribution of the subgrid flux (or the flux enhancement) at each tested resolution is given by

$$\mathbf{S}_g = \frac{[\mathbf{F}_{\text{subgrid}}]}{[\mathbf{F}_{\text{true}}]}. \quad (19)$$

Our observational estimate of the composite subgrid velocity scale, $[V_{\text{sg}}]$, is calculated for each resolution using

$$V_{\text{sg}} = [(\langle U \rangle^2 - V^2)^{1/2}], \quad (20)$$

where U and V have been defined in Eqs. (5) and (9), respectively.

For comparison to other studies, and for comparison to our two-dimensional grid-box analysis, we also evaluate a subgrid velocity scale on the basis of one-dimensional low-level flight tracks. In this case, the angle brackets refer to a 1D spatial average, in contrast to the 2D spatial averaging described earlier in this section. Electra flight legs 80 km in length were used to evaluate V_{sg} at grid scales of 40 and 80 km. In this case, each 80-km flight leg provides one estimate of the 80-km grid scale based on eight local 10-km means, and two estimates of the 40-km grid scale based on four local 10-km means. In the 1D case, all the grid-scale estimates are based on independent observations and the compositing is done using a simple average over all estimates. From the Electra flight days in Table 1, we find 63 cases of 80-km flight legs on eight different flight days.

5. Observed subgrid flux and velocity scale

Our observational estimates of the true and model fluxes as a function of grid scale for fair weather con-
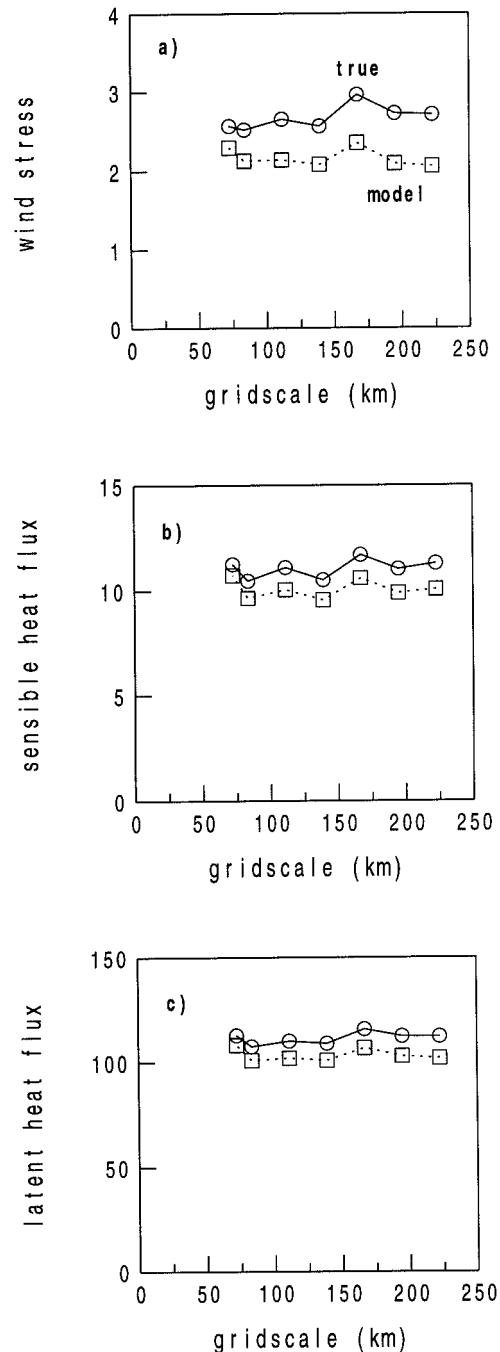

FIG. 3. Observational estimates of the "model" (squares and dashed) and "true" (circles and solid) two-dimensional grid-box average surface fluxes as a function of grid scale (km) for (a) scalar wind stress ($\times 10^{-2}$ m^2 s^{-2}), (b) sensible heat (W m^{-2}), and (c) latent heat (W m^{-2}).

ditions are shown in Figs. 3a–c. The relative subgrid enhancement of the flux, $\mathbf{S}_g$, is shown in Figs. 4a–c. At a resolution of 2.0, that is, a spatial scale of approximately 220 km × 220 km, the relative subgrid enhancements of the sensible heat flux, latent heat flux, scalar
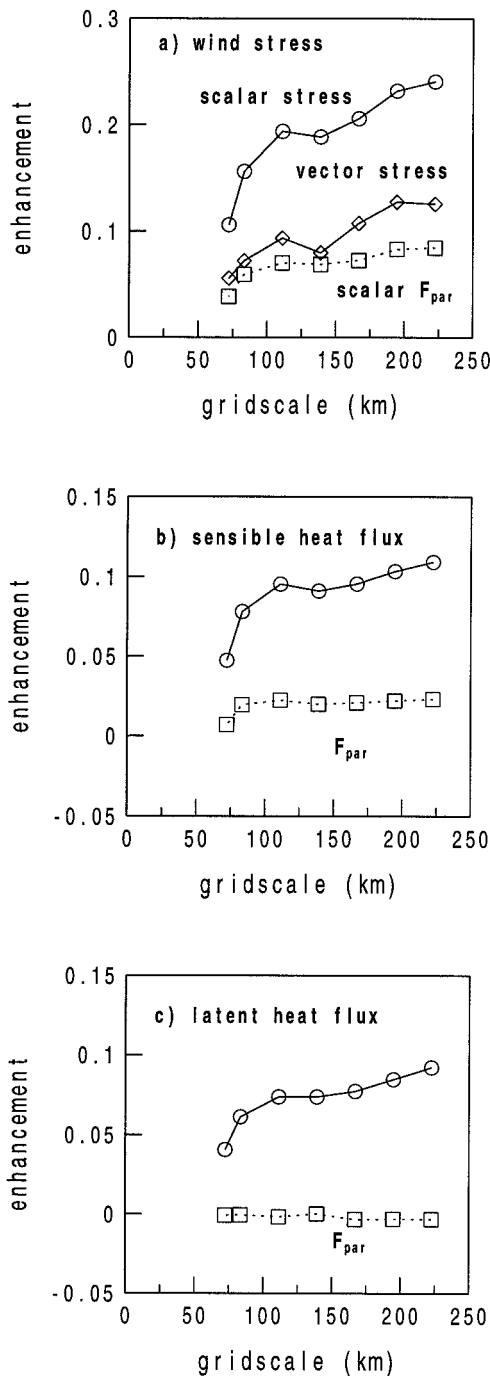
FIG. 4. Observational estimates of the relative subgrid flux enhancement (as a fraction of the "true" flux) from the two-dimensional gridbox average surface fluxes for $\mathbf{F}_{model}$ (solid lines) and $\mathbf{F}_{par}$ (dashed lines) as a function of grid scale (km) for (a) scalar (circles) and vector (diamonds) wind stress, (b) sensible heat, and (c) latent heat.

wind stress, and vector wind stress magnitude are 11%, 9%, 24%, and 12%, respectively (Figs. 4a–c). The composite results in Figs. 3a–c and 4a–c are based on 15, 21, 23, 23, 21, 22, and 20 1-h realizations for each grid box resolution of 0.65, 0.75, 1.0, 1.25, 1.5, 1.75, and

2.0, respectively, on seven different days. The number of grid boxes included in a single 1-h realization ranges from 1 to approximately 200 grid boxes.

Most of the subgrid flux is due to the subgrid directional variability of the wind field. We demonstrate this by supposing that we have a model that contains a perfect parameterization of the subgrid velocity scale V_{sg} and hence $\langle U \rangle$. The parameterized grid-box average fluxes $\mathbf{F}_{par}$ from our hypothetical model may then be written as

$$\mathbf{F}_{par} = \mathcal{F}(\langle U \rangle, \langle \overline{\theta}_{sfc} \rangle, \langle \overline{\theta} \rangle, \langle \overline{q} \rangle). \qquad (21)$$

The error $\mathbf{F}_{true} - \mathbf{F}_{par}$ expressed as a fraction of $\mathbf{F}_{true}$ is 2% for the sensible heat, -0.3% for the latent heat, and 8% for the scalar wind stress, at a resolution of 2.0 (Figs. 4a–c). The residual in this case is entirely due to nonlinearities in the transfer coefficients and nonzero covariance between the individual terms in the bulk formula [see e.g., Ledvina et al. (1993) and Esbensen and McPhaden (1996)]. This result suggests that most of the subgrid flux could be effectively parameterized in terms of a subgrid velocity scale, and that the covariance terms are of lesser importance, at least for relatively undisturbed conditions over the Pacific warm pool.

The scalar wind stress is the appropriate stress for estimating the surface friction velocity u_* required for upper ocean mixing calculations, while the vector wind stress drives organized oceanic circulations by systematic directional forcing at the atmosphere–ocean boundary.

In agreement with observational results reported in Mahrt and Sun (1995b) and Sun et al. (1996), the subgrid enhancement of the scalar wind stress is larger than the enhancement of the sensible or latent heat flux at all resolutions tested. This is because the subgrid variability of the wind components is the primary effect generating subgrid flux enhancement, and this effect is squared in the bulk formula for the scalar wind stress,

$$F_\tau = \rho C_d U^2, \qquad (22)$$

where C_d is the drag coefficient. The subgrid scalar wind stress also has a significant contribution from the covariance between the drag coefficient and the wind speed because the drag coefficient in the COARE algorithm is more highly wind speed dependent than the transfer coefficients for heat or moisture.

We also estimated the subgrid enhancement of the vector stress by calculating the two stress components separately using the COARE algorithm and applying the grid-box and compositing analyses discussed above. The vector wind stress was then formed from the composited components.

The observed subgrid enhancement of the vector wind stress is considerably less than the enhancement of the scalar wind stress (Fig. 4a). The vector stress enhancement can be represented by the difference in magnitude alone since the difference in direction between the true and model vector stress is small (less than 5°) for the
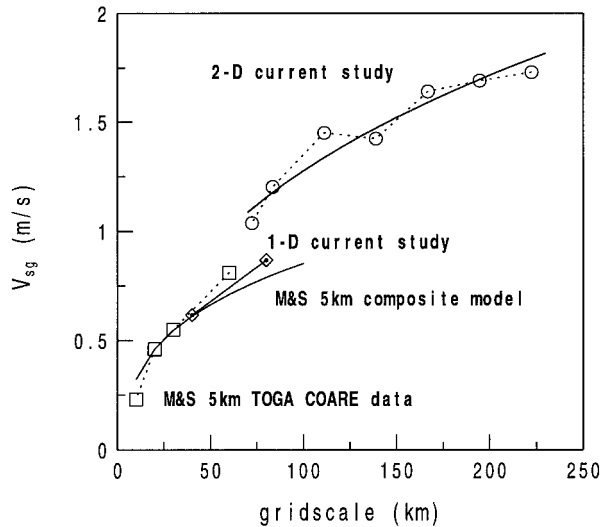
FIG. 5. The subgrid velocity scale (m s^{-1}) as a function of grid scale (km) for our two-dimensional grid-box estimates (circles and dashed), our 1D flight track estimates (diamonds and solid), and 1D flight track estimates from Mahrt and Sun (1995a) for TOGA COARE Electra (squares and dashed). The upper solid curve is the least squares fit to our 2D estimates [Eq. (24)]. The lower solid curve is the composite least squares model of Mahrt and Sun (1995a) based on 1D aircraft flight tracks from five different field experiments.

datasets considered here. As expected, the vector wind stress enhancement is much less than the scalar stress enhancement because the correlation of wind components with the scalar wind speed is much less than the correlation of the wind speed with itself. The observed subgrid enhancement of the vector wind stress is similar to that found for the sensible heat and latent heat fluxes on these space and time scales. Note that this is not the case on longer (e.g., monthly) timescales (Esbensen and Reynolds 1981).

Our observational estimate of the subgrid velocity scale [Eq. (20)] increases with grid scale from 1.0 m s^{-1} at a grid scale of 72 km to 1.7 m s^{-1} at a grid scale of 222 km (Fig. 5). For comparison, the one-dimensional flight track estimates are 0.6 m s^{-1} at 40 km and 0.9 m s^{-1} at 80 km (Fig. 5). The one-dimensional result for V_{sg} agrees with a similar one-dimensional analysis of TOGA COARE Electra data reported in Mahrt and Sun (1995a), which used a local averaging scale of 5 km instead of the current value of 10 km, to estimate V_{sg}. A grid-scale-dependent parameterization of V_{sg} by Mahrt and Sun (1995a) from an observational study of several diverse aircraft datasets, including four over land and the TOGA COARE Electra set, and all using 5-km local averaging and 1D flight tracks, also agrees with our 1D result (Fig. 5).

The subgrid flux is a nonlinear function of the subgrid velocity. Our observational estimate of V_{sg} using Eq. (20) is not unique. An alternate compositing method was tested

$$V_{sga} = ([\langle U \rangle]^2 - [V]^2)^{1/2}. \qquad (23)$$

This alternate form yields a composite subgrid velocity that is larger than the estimate found using Eq. (20) by about 0.2 m s^{-1} at all resolutions tested. A calculation of the subgrid flux enhancement using a grid-scale-dependent V_{sg} parameterization [Eq. (24) below] based on the estimate of V_{sg} using Eq. (20) and the estimate using the alternate form [Eq. (23)] shows that Eq. (20) slightly underpredicts V_{sg} and that the alternate form slightly overpredicts V_{sg}. Neither compositing method is generally superior to the other, and we choose V_{sg} from Eq. (20) rather than (23) for the remaining discussions.

The larger subgrid velocity scale found using the 2D grid-box analysis, as compared to the 1D analysis, can be explained by noting that the variation of the flow within the grid box is neither homogeneous nor isotropic in general, even for relatively undisturbed conditions. The flow is characterized by large mean gradients and coherent structures on scales comparable to the grid scale. When the flow is not homogeneous and isotropic, a 1D flight track may capture all or none of the subgrid velocity variations, depending on the relative orientation of the flight track to the large-scale wind gradients. Thus, in the composite, the subgrid velocity scale from a 1D analysis must be less. If we assume that a 1D flight track has a representative cross-track width of 25 km, regardless of flight track length, then the 2D and 1D estimates of V_{sg} agree when plotted versus grid-box area.

Examples of the horizontal wind flow field observed by the aircraft on two different flight days are shown in Figs. 6 and 7. These two cases are characterized by large subgrid flux (and subgrid velocity scale) and excellent spatial grid-box coverage. The flow on 16 December (Fig. 6) is characterized by strong southwesterly-to-westerly winds, while on 9 January (Fig. 7) the winds are much weaker and from the northeast to southeast. In the former case, the primary feature of the flow is a gradual turning of the wind, while in the later it is the north–south convergence. While the large-scale features of the flow are quite different on these two days, the subgrid flux and subgrid velocity observed for each is larger than average.

The well-behaved increase in V_{sg} with grid scale suggests a simple grid-scale dependent model of the form

$$V_{sg} = a \left(\frac{\Delta X}{10 \text{ km}} - 1 \right)^b, \qquad (24)$$

where ΔX is the grid scale in kilometers and represents a square grid box of area ΔX^2 (Mahrt and Sun 1995a). Note that the subgrid velocity is zero when ΔX is 10 km, our local averaging scale. Least squares regression using our seven composite data points, representing seven different grid scales, yields $a = 0.53$ m s^{-1} and $b = 0.40$ with an R^2 of 0.93 (Fig. 5). Our coefficients a and b are larger than those reported by Mahrt and Sun (1995a) of 0.32 and 0.33, respectively, which were based on their 1D flight track estimates of V_{sg} using
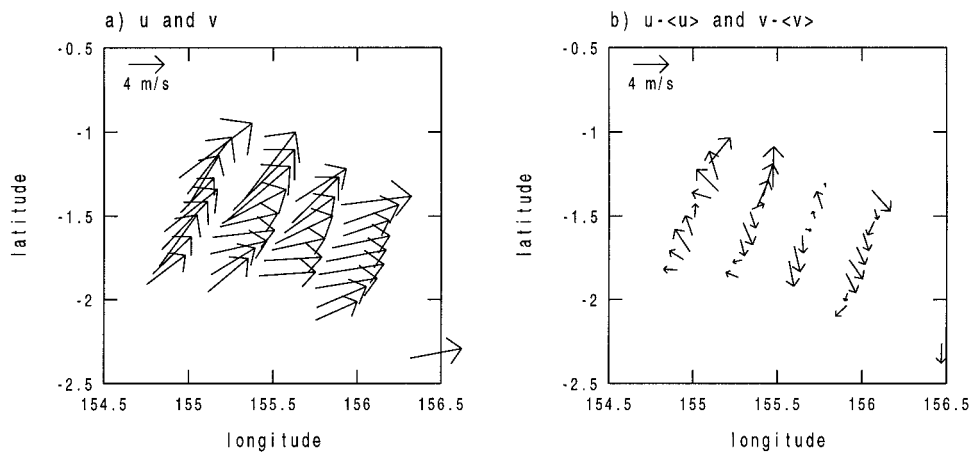
FIG. 6. The near-surface wind field on 16 December 1992 from low-level aircraft observations made within a 1-h period for (a) observed wind vectors and (b) grid-box deviation wind vectors. The grid-box deviation wind components are $u - \langle u \rangle$ and $v - \langle v \rangle$, where the angle brackets refer to a spatial average over the grid-box domain.

several aircraft datasets over land and water. The larger V_{sg} from our 2D grid-box analysis may be due in part to the additional subgrid velocity inherent in a 2D versus a 1D observational estimate.

Even if the subgrid flux enhancement were entirely due to wind direction variability, that is, the difference between $\langle U \rangle$ and V, the subgrid velocity parameterization [Eq. (24)] would not be guaranteed to represent the subgrid flux enhancement because the flux is a nonlinear function of the subgrid velocity scale. The grid-scale-dependent V_{sg} parameterization was tested by calculating the grid-box average fluxes using Eq. (24). The V_{sg} parameterization is implemented by substituting $(V^2 + V_{sg}^2)^{1/2}$ for V in the $\mathbf{F}_{model}$ representation. The differences between the surface fluxes calculated with the V_{sg} parameterization minus the $\mathbf{F}_{par}$ representation for the 2.0

resolution composite are less than 1% for the scalar wind stress, sensible heat flux, and latent heat flux. This confirms that the grid-scale-dependent V_{sg} model effectively parameterizes the subgrid directional variability of the wind field for this dataset.

The variability of the observed daily mean subgrid velocity scale for the seven different days is shown in Fig. 8. The standard error of each daily mean estimate is about 0.2 m s^{-1}. The range of the mean daily V_{sg} estimates at a grid scale of 222 km is 0.83–2.25 m s^{-1}. Comparison of V_{sg} for the seven different days shows that the rate of increase of V_{sg} with grid scale is approximately the same, although the subgrid velocity can have quite different values on different days. The best fit to the composite subgrid velocity (the solid line in Fig. 8) is not necessarily the best fit to the average of
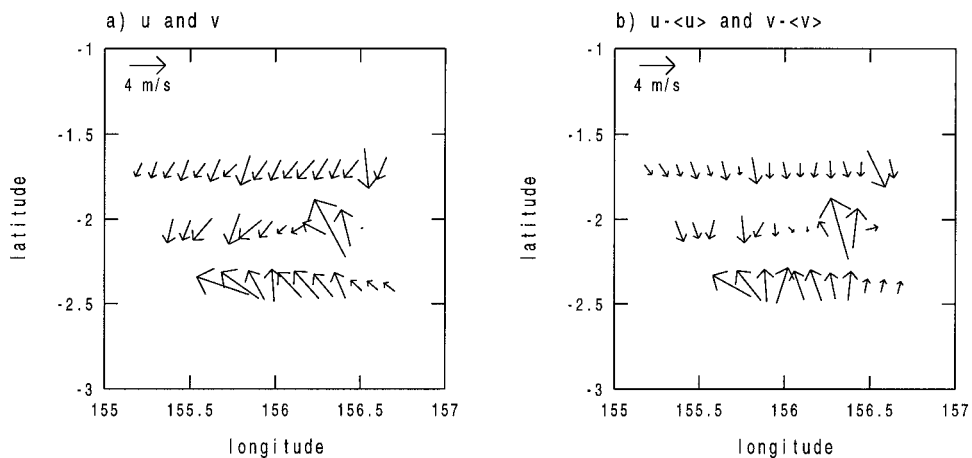

FIG. 7. The near-surface wind field on 9 Jan 1993 from low-level aircraft observations made within a 1-h period for (a) observed wind vectors and (b) grid-box deviation wind vectors. The grid-box deviation wind components are $u - \langle u \rangle$ and $v - \langle v \rangle$, where the angle brackets refer to a spatial average over the grid-box domain.
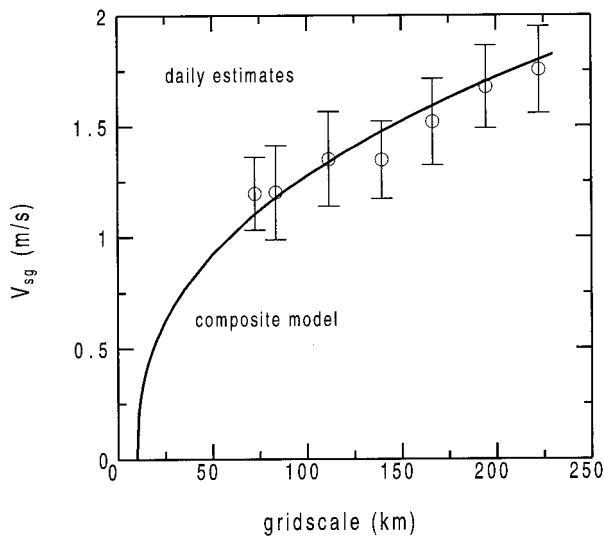
FIG. 8. Daily variability of the subgrid velocity scale (m s^{-1}) as a function of grid scale (km) for our two-dimensional grid-box estimates. The circles and error bars show the mean plus and minus one standard error of the seven individual daily mean estimates. The solid line is the least squares fit [Eq. (24)] to the composite 2D grid-box estimates.

FIG. 9. The subgrid velocity scale (m s^{-1}) as a function of grid scale (km) for the *Moana Wave* observations during disturbed (squares) and undisturbed (circles) conditions. The error bars show plus and minus one standard error. The solid line is the least squares fit [Eq. (24)] to the composite 2D grid-box estimates.

the daily means, since each day has a different number of 1-h realizations in the composite.

6. Conclusions and discussion

We have made observational estimates of the portion of the areally averaged surface fluxes that would be unresolved in a large-scale numerical model under fair weather conditions. The results show that the subgrid flux enhancement increases with grid-box area and that most of the discrepancy can be explained by unresolved directional variability in the near-surface wind field within the simulated grid box. Maps of the observed wind fields show that the directional variability includes not only contributions from fair weather convective bands and patches, but also contributions from curvature and speed variations of the large-scale flow across the grid box. The inclusion of a grid-scale dependent subgrid velocity scale in the bulk aerodynamic formulas was found to effectively parameterize the subgrid flux enhancement due to directional variability in the wind field.

A one-dimensional observational estimate of the subgrid velocity scale derived from Electra flight legs was found to be consistent with the results of Mahrt and Sun (1995a). The subgrid velocity scale estimated from one-dimensional aircraft samples is smaller than that derived from a two-dimensional grid-box analysis. The additional enhancement in the 2D case is caused by the nonhomogeneous and nonisotropic characteristics of the subgrid-scale wind variability.

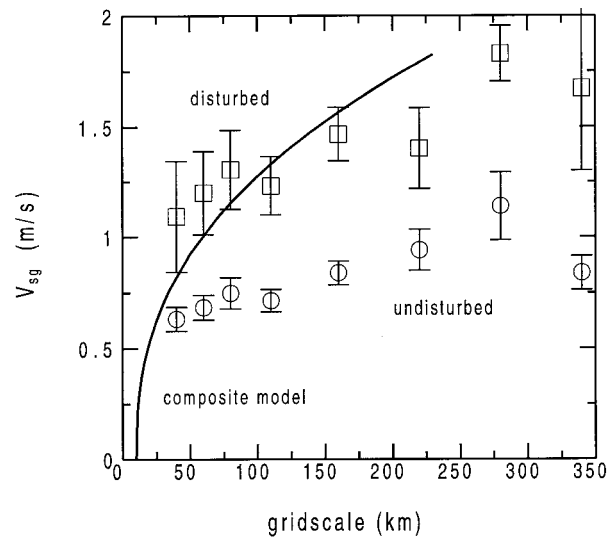Our aircraft-based observations of the subgrid fluxes and subgrid velocity scale were restricted to days with

undisturbed conditions (class 0 or 1 convective activity) over the western Pacific warm-pool region. This restriction was necessary to avoid severe spatial sampling problems during disturbed conditions. We expect, however, that the subgrid flux enhancement will be dependent on the degree and nature of convective activity as well as the grid scale.

To illustrate the possible dependence of the subgrid velocity scale on convective activity, we calculated estimates of the subgrid velocity in disturbed and undisturbed conditions using the *Moana Wave* (Fig. 9) and IMET mooring (not shown). The results for both surface-based platforms are similar. The subgrid velocity scale was evaluated using Eq. (20) where the angle brackets now represent a time average representing a one-dimensional spatial grid scale. For the purpose of estimating the disturbed subgrid velocity scale, these surface-based platforms have the advantage of a relatively long and continuous record of observations, compared with the aircraft dataset. A disadvantage of the surface platforms is that they only "see" upwind conditions that are advected past the platform, and thus do not directly sample spatial variability. The grid scale for the surface platforms (Fig. 9) is calculated using the observed velocity *V* as an advective velocity scale. The subgrid velocity was evaluated for time averaging periods of 4, 8, 12, and 24 h, and the time averages were converted to 1D spatial averages using the observed advective velocity scale. A time averaging scale of 4 h represents about four 50-min observations of the local mean wind components for the *Moana Wave* and about 32 7.5-min observations for the IMET mooring. We have used the precipitation measured on the *Moana*

Wave as an indicator of convective activity in the area, and classify each time average as disturbed when the average rainfall rate exceeds 0.1 mm h^{-1}. This threshold value is selected to ensure a reasonable number of disturbed periods, and serves only to partition the data into more disturbed and less disturbed categories.

For grid scales less than about 100 km, our aircraft-based 2D grid-box estimate of the subgrid velocity lies between the surface-based undisturbed and disturbed estimates. At grid scales larger than 100 km, the 2D grid-box estimate of V_{sg} is generally equal to or larger than the surface-based platform estimates. For the subgrid velocities calculated from the *Moana Wave* and IMET mooring, the increase of V_{sg} for disturbed compared to undisturbed conditions ranges from about 0.4 to 0.8 m s^{-1}, and generally increases with grid scale. The relatively small subgrid velocities observed by the surface platforms compared to the 2D grid-box estimates, especially for undisturbed conditions and large grid scale, may be due to the difference between spatial variability of the wind as measured by the aircraft, and the temporal variability of the wind blowing past a fixed spatial location. The surface platform estimates of V_{sg} may be more closely related to the smaller 1D aircraft-based estimates.

The difference in the subgrid velocity scale for disturbed and undisturbed conditions in this study is consistent with the monthly averaged evaporative and sensible heat flux enhancements computed by Esbensen and McPhaden (1996) over the equatorial Pacific. They found that the flux enhancements were small in regions with little precipitation. In regions with significant precipitation, the flux enhancements were much larger, although there was not a systematic relationship between the magnitude of the flux enhancement and the precipitation.

REFERENCES

Beljaars, A. C., 1995: The parameterization of surface fluxes in large scale models under free convection. *Quart. J. Roy. Meteor. Soc.,* **121,** 255–270.

Esbensen, S. K., and R. W. Reynolds, 1981: Estimating monthly averaged air–sea transfers of heat and momentum using the bulk aerodynamic method. *J. Phys. Oceanogr.,* **11,** 457–465.

——, and M. J. McPhaden, 1996: Enhancement of tropical ocean evaporation and sensible heat flux by atmospheric mesoscale systems. *J. Climate,* **9,** 2307–2325.

Fairall, C. W., E. F. Bradley, D. P. Rogers, J. B. Edson, and G. S. Young, 1996: Bulk parameterization of air–sea fluxes for Tropical Ocean–Global Atmosphere Coupled-Ocean Atmosphere Response Experiment. *J. Geophys. Res.,* **101,** 3747–3764.

Godfrey, J. S., and A. C. M. Beljaars, 1991: On the turbulent fluxes of buoyancy, heat and moisture at the air–sea interface at low wind speeds. *J. Geophys. Res.,* **96,** 22 043–22 048.

Johnson, R. H., and M. E. Nicholls, 1983: A composite analysis of the boundary layer accompanying a tropical squall line. *Mon. Wea. Rev.,* **111,** 308–319.

Ledvina, D. V., G. S. Young, R. A. Miller, and C. W. Fairall, 1993: The effect of averaging on bulk estimates of heat and momentum fluxes for the tropical western Pacific Ocean. *J. Geophys. Res.,* **98,** 20 211–20 217.

Mahrt, L., and J. Sun, 1995a: The subgrid velocity scale in the bulk aerodynamic relationship for spatially averaged scalar fluxes. *Mon. Wea. Rev.,* **123,** 3032–3041.

——, and ——, 1995b: Dependence of the surface exchange coefficients on averaging scale and grid size. *Quart. J. Roy. Meteor. Soc.,* **121,** 1835–1852.

——, D. Vickers, J. Howell, J. Højstrup, J. M. Wilczak, J. Edson, and J. Hare, 1996: Sea surface drag coefficients in the Risø Air Sea Experiment. *J. Geophys. Res.,* **101,** 14 327–14 335.

Sun, J., J. F. Howell, S. K. Esbensen, L. Mahrt, C. M. Greb, R. Grossman, and M. A. LeMone, 1996: Scale dependence of air–sea fluxes over the western equatorial pacific. *J. Atmos. Sci.,* **53,** 2997–3012.

Vickers, D., and L. Mahrt, 1997: Quality control and flux sampling problems for tower and aircraft data. *J. Atmos. Oceanic. Technol.,* **14,** 512–526.

Williams, A. G., H. Kraus, and J. M. Hacker, 1996: Transport processes in the tropical warm pool boundary layer. Part I: Spectral composition of fluxes. *J. Atmos. Sci.,* **53,** 1197–1202.

World Climate Research Program, 1990: Scientific plan for the TOGA Coupled Ocean–Atmosphere Response Experiment. World Climate Res. Program Publ. Series, WMO/TD-64, Vol. 3, 105 pp.